

Model description of electron transfer between PTCDA molecule and metal surface upon molecular adsorption and STM manipulation

Andrei G. Borisov *

Institut des Sciences Moléculaires d'Orsay (ISMO), UMR 8214, CNRS, Université Paris-Saclay, 91405 Orsay Cedex, France and DIPC, Paseo Manuel de Lardizabal 5, Donostia, San Sebastián 20018, Spain



(Received 28 April 2024; revised 2 July 2024; accepted 19 July 2024; published 9 August 2024)

The coupling between the molecule-localized electronic states and continuum of the electronic states of the metal surface is of paramount importance for adsorption dynamics, surface reactivity, as well as for the electron- and photon-induced processes at metal surfaces. Here, using the model one-active-electron description and wave-packet propagation approach, we study the resonant electron transfer between the perylene-tetracarboxylic-dianhydride (PTCDA) molecule and metal substrate from 0.5 nm separations down to the adsorption distances. We also address the situation where the molecule is lifted up from the substrate using the scanning tunneling microscope. A detailed comparison with the large amount of available experimental data and *ab initio* calculations allows us to discuss the validity of the method and the main robust effects driving the lifetimes of molecule-localized states that it reveals. Thus we show that the symmetry of molecule-localized states strongly impacts the dependence of the electron transfer rates on the metal band structure and molecule-surface distance. In addition, in full agreement with recent experimental data on scanning tunneling microscopy manipulation where an adsorbed molecule is lifted into the vertical geometry, we find an order of magnitude reduction of the adsorbate-substrate coupling.

DOI: [10.1103/PhysRevB.110.075413](https://doi.org/10.1103/PhysRevB.110.075413)

I. INTRODUCTION

When atomic or molecular species interact with metal surfaces, the atom- or molecule-localized electronic states are coupled with a continuum of the propagating electronic states of the metal. As a result, an electron (or a hole) can be transferred between an atom/molecule and the metal via the resonant charge transfer (RCT) process. The atom- or molecule-localized electronic states become quasi-stationary states (QSSs), or resonances, characterized by their energies and widths given by the RCT rates. In the case of the atomic and molecular projectiles, the RCT determines, e.g., charge states of the projectiles, molecular sticking to the surface, and electronic excitations [1–7]. For the adsorbates, the energies and widths (inverse of the lifetimes) of the QSSs [8–13] are the key parameters for many processes at surfaces such as reactivity, energy harvesting, electron transport, and electron-photon coupling in molecular functionalized tunneling devices [14–22]. Thus, RCT that is too fast harms the energy transfer from excited QSSs to other deexcitation channels and might quench, e.g., photon emission or, similarly, surface reactivity [21–27].

To control, and in particular to increase, the lifetime of the QSSs, the spacer layers such as ionic crystals, hexagonal boron nitride, or oxides are typically used, allowing one to decouple the electronic states of an adsorbate and a substrate [24,28–33]. This opens interesting perspectives in using scanning probes to manipulate charges of adsorbed species

and to control atomic rearrangements and reactions [34–42]. In addition, it enables the photon emission from the functionalized scanning tunneling microscopy (STM) junctions following excitation by light or tunneling electrons [43–48]. Photo- or electro-stimulated light emission has attracted much interest in recent years, in particular in the context of hyper-resolved photon maps from a single molecule [47,49–52]. For large aromatic molecules, the decoupling can also be reached by changing the adsorption geometry from the flat (with molecular plane parallel to the surface plane) to standing upright or suspended between the substrate and the tip of a STM [53–57].

The importance of the molecule-metal surface charge transfer for multiple phenomena involving gas-phase and adsorbed species leads to the need for theoretical support to explain and program experiments. In this context, the *ab initio* approaches typically based on the density functional theory (DFT) calculations [12,58–63] for the adsorption, and on the nonequilibrium Green's function technique for the (inelastic) transport in molecular junctions [64–67], stand alone as the state of the art in the field. Nonetheless, an *ab initio* strategy might be numerically heavy, e.g., in the situations when the large size of the supercell is needed to describe a single adsorbate and to avoid adsorbate-adsorbate interactions, or when the decoupling spacer layers [32,33] or molecule-surface distance of some Å result in the long lifetimes and thus narrow width of the adsorbate- or projectile-localized electronic states.

The examples above prove an interest in model approaches to grasp the main physical effects that control the electronic coupling between an adsorbate and a substrate. One such

*Contact author: andrei.borisov@universite-paris-saclay.fr

approach is based on the one-active-electron approximation. An “active” orbital is isolated within the wave function of the projectile or adsorbate corresponding to the given many-body state. An electron tunneling is seen as a one-electron energy-conserving transition between this orbital and electronic states of the metal, i.e., the RCT. The stationary or time-dependent one-electron calculations are performed to find and characterize the energy of the “active” orbital and the electron transfer rate. Obviously, strongly correlated systems, such as Kondo resonance or inelastic tunneling [65–68], cannot be addressed within this approximation and require explicitly many-body treatments [69–71]. However, when the decomposition of the many-body state on the active orbital(s) and spectator part is possible, the one-active-electron approximation often allows for a quantitative description of experiments addressing an excited electron dynamics, and electron transfer for atomic species interacting with metal surfaces [3,4,10,59,72]. Recently, we introduced the wave-packet propagation (WPP) approach to describe the electron transfer between organic molecules and metallic substrates within the one-active-electron approximation [73–75]. The method is built on earlier studies of atomic adsorbates [10], and it is based on the rigorous solution of the one-electron time-dependent Schrödinger equation (TDSE) to obtain the characteristics of the active orbital such as its energy and width determined by an effective one-electron potential of the system.

Here, using the WPP description of the RCT, we address the electron coupling between a large planar chromophore molecule and metal substrate. Specifically, we study the 3,4,9,10-perylene-tetracarboxylic-dianhydride (PTCDA) interacting with the Ag(111) surface, as sketched in Fig. 1. The results presented in this work are obtained using different model descriptions of the metal substrate and span molecule-surface distances ranging from an adsorption distances to 0.5 nm above metal. Along with visualization of the decay dynamics provided by WPP, this allows a detailed discussion of the main effects determining the RCT rates and energies of the molecule-localized resonances. In particular, we analyze the effect of the projected band structure of the metal and its dependence on the symmetry of molecular states. Furthermore, we study the effect of molecular orientation on the evolution of the coupling strength between the lowest unoccupied molecular orbital (LUMO) and the surface upon lifting PTCDA from the Ag(111) substrate as recently reported [62,63,70]. It is important to stress that the PTCDA adsorption on Ag(111) has been thoroughly studied in the surface science community [54,61,63,76–79], and recently it has been in a focus of the scanning tunneling microscopy studies of the single-molecule luminescence probed on the atomic scale [47,80]. Thus, the validity of our conclusions can be confirmed by the semiquantitative agreement between the WPP results and the experimental and *ab initio* data.

The paper is organized as follows. In Sec. II, we outline the model description of the resonant charge transfer between the adsorbed molecule and metal substrate. Section III is devoted to the discussion of the WPP results and their comparison with experimental data. Section IV presents the summary and conclusions.

Atomic units are used throughout this paper, unless otherwise stated.

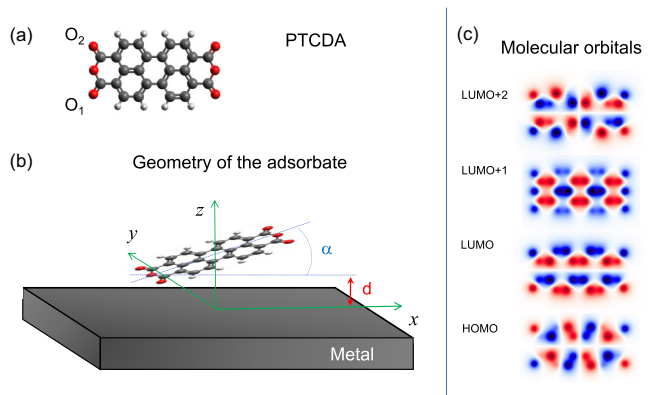


FIG. 1. Sketch of the studied system. (a) The atomic structure of the planar PTCDA molecule consisting of oxygen (red), carbon (dark gray), and hydrogen (light gray) atoms. (b) The geometry of the adsorbate-substrate system. The adsorption distance d is measured between the image plane of the metal and closest atoms of the PTCDA (oxygen atoms). The molecular plane rotates by the angle α around the axis given by the O_1 and O_2 atoms. For $\alpha = 0$, the geometry corresponds to the molecule adsorption on Ag(111) [76], and varying α represents molecule manipulation with a STM tip [62,63,70]. (c) The wave function of the highest occupied molecular orbital (HOMO), LUMO, LUMO+1, and LUMO+2 molecular orbitals calculated with wave-packet propagation for the freestanding PTCDA molecule. Results are shown at 1 a.u. above the molecular plane to avoid the node of the wave function of the π electron system. The red (blue) color stands for the positive (negative) values.

II. ONE-ELECTRON DESCRIPTIONS OF THE RESONANT CHARGE TRANSFER BETWEEN ADSORBED MOLECULE AND METAL SUBSTRATE

A. The wave-packet propagation

Our description of the RCT between the PTCDA molecule and metal substrate builds on earlier developments of the WPP approach [10,73–75]. Essentially, one calculates the energies and widths (RCT rates) of the active molecular orbitals broadened into the resonances because of the coupling with metal. To this end, one considers that an electron active in RCT is transferred between molecular and metallic wells of an effective one-electron potential. The electron dynamics is addressed directly in the time domain. We outline here the main ingredients of the method.

The wave function of an electron active in RCT, $\psi(\vec{r}, t)$, evolves in time according to the TDSE,

$$i \frac{\partial}{\partial t} \psi(\mathbf{r}, t) = [\hat{T} + V(\mathbf{r})] \psi(\mathbf{r}, t), \quad (1)$$

where $\hat{T} = -\frac{1}{2}\nabla^2$ is the kinetic energy operator, and $V(\mathbf{r})$ is the one-electron effective potential detailed below.

The time-dependent wave function $\psi(\mathbf{r}, t)$ and potential $V(\mathbf{r})$ are represented on a three-dimensional (3D) mesh of equidistant points in (x, y, z) coordinates, which allows us to use the Fourier-grid pseudospectral approach [81–85] for the kinetic energy operator. In the x , y , and z directions, the mesh typically comprises 1024 nodes with 0.11 a.u. spatial step. The initial condition $\psi_0(\mathbf{r}) \equiv \psi(\mathbf{r}, t = 0)$ is

often given by the orbital of the freestanding molecule identified as an orbital active in RCT; however, other choices are also possible [10]. The $\psi(\mathbf{r}, t)$ is obtained using the short-time split-operator propagation scheme [81,82], with time step $\Delta t = 0.025$ a.u. (~ 0.6 as). Finally, analysis of $\psi(\mathbf{r}, t)$ provides resonance energies E_m , charge transfer rates Γ_m (or resonance widths), and energy-resolved wave functions $\psi(\mathbf{r}, E_m)$, $m = (\text{LUMO}, \text{LUMO} + 1, \text{LUMO} + 2)$ of the active molecular orbitals broadened into the resonances by an interaction with the substrate [10,73]. Thus, the autocorrelation function $A(t) = \iiint \psi_0^*(\mathbf{r})\psi(\mathbf{r}, t)d^3\mathbf{r}$ can be used to obtain the projected density of electronic states as function of electron energy E ,

$$n(E) = \frac{1}{\pi} \text{Re} \left\{ \int_0^\infty A(t) e^{iE_m t} dt \right\}. \quad (2)$$

$\text{Re}\{Z\}$ stands for the real part of the complex number Z . The molecule-localized quasistationary states appear as resonances in $n(E)$ and their energies and decay rates can be obtained from the resonance energies and widths. Alternatively, the autocorrelation function can be fitted by the sum of decaying exponentials, $A(t) = \sum_j a_j e^{-i(E_j - i\Gamma_j/2)t}$. Here, for some j corresponding to the contribution of the quasistationary states, E_j and Γ_j converge with number of terms and maximum propagation time. The resonance wave function is obtained as

$$\psi(\mathbf{r}, E_m) = \frac{1}{\pi} \int_0^\infty \psi(\mathbf{r}, t) e^{iE_m t} dt, \quad (3)$$

and it allows an intuitive visual insight into the RCT process (see below).

B. The model one-electron potential

An effective one-electron potential of the system is a model potential given by a sum of several terms: the electron-molecule interaction $V_M(\mathbf{r})$, the electron interaction with metal substrate $V_S(z)$, the change of the electron-metal interaction because of the presence of the molecule $\Delta V_S(\mathbf{r})$, and the absorbing potential $V_a(\mathbf{r})$,

$$V(\mathbf{r}) = \begin{cases} V_M(\mathbf{r}) + V_S(z) + \Delta V_S(\mathbf{r}) + V_a(\mathbf{r}), & z \geq 0 \\ V_S(z) + V_a(\mathbf{r}), & z < 0. \end{cases} \quad (4)$$

The electron-molecule and electron-metal model potentials are set independently for the gas-phase molecule at infinite separation from the metal and for an infinite perfect metal without an adsorbate. Using z axis perpendicular to the surface, the metal is located at $z < 0$, and the metal/vacuum interface $z = 0$ corresponds to the position of the image plane of the metal. For Ag(111), it is located at 2.2 a.u. (1.17 Å) above the plane of the surface atoms [86]. As follows from Eq. (4), the model employed here enforces full screening of the electron-molecule interaction $V_M(\mathbf{r})$ inside the metal for $z \geq 0$. Below we explain the different potential terms.

The *electron-molecule interaction potential* $V_M(\mathbf{r}) = V^L(\mathbf{r}) + V^{NL}(\mathbf{r})$ is calculated for the freestanding PTCDA with equilibrium geometry of the neutral molecule [87], i.e., we neglect atomic rearrangements upon adsorption [88–90] and STM manipulation [62,63,70]. This choice, however, is

not mandatory and one can use molecular geometries determined *ab initio* to account for atomic rearrangements at the price of making the methodology numerically heavier. The local $V^L(\mathbf{r})$ and nonlocal $V^{NL}(\mathbf{r})$ contributions are obtained from the *ab initio* quantum chemistry density functional theory (DFT) calculations within the local density approximation with Perdew-Wang correlation energy [91], as implemented in the ABINIT package [92]. The local potential is given by the sum of Hartree and exchange-correlation potentials. The nonlocal potential in the Kleyman-Bylander form [93] represents an electron interaction with cores of individual atoms forming the molecule.

It is important that the energies E_m of the active orbitals are representative for the energies of the many-body states with respect to the vacuum level and the Fermi energy of the substrate, E_F . Indeed, the Fermi statistics is introduced *ad hoc a posteriori* by requiring that the RCT rates Γ_m calculated within the one-electron approximation characterize an electron loss into the metal for the active orbitals with energies above E_F , and an electron capture from the metal (subject to the spin statistics) for the active orbitals with energies below E_F . Considering the charge transfer dynamics, the method therefore does not apply in the situations where the finite-temperature effects are important. It is worth noting that an electron capture from the metal can be alternatively presented as a hole loss into the metal, which appears to be handy in certain situations.

It follows from the experimental data that the PTCDA molecule is adsorbed on the Ag(111) surface as an anion with occupied LUMO resonance located below the Fermi level [61,76,80,88,89,94,95]. Since the molecular anion is formed by an electron attachment to the neutral molecule, for the freestanding PTCDA, the binding energy of the LUMO with respect to the vacuum level should represent the electron affinity E_a . However, since Koopmans' theorem [96] does not apply for the DFT, the ABINIT results (4.9 eV) fail to reproduce the data reported in the literature (3.25 eV [97], 3.07 eV [98]). In some cases, the agreement can be improved by using complex density functionals; however, in order to efficiently apply the WPP technique, we use a different strategy. Based on the results reported in Ref. [97], we set the $V^L(\mathbf{r})$ potential as follows:

$$V^L(\mathbf{r}) = \zeta V_0^L(\mathbf{r}) + (1 - \zeta) V_-^L(\mathbf{r}), \quad (5)$$

where $V_0^L(\mathbf{r})$ is the local potential obtained with ABINIT for the freestanding neutral molecule, and $V_-^L(\mathbf{r})$ is the local potential calculated for the freestanding molecular anion with geometry given by that of the neutral molecule, and assuming 1/2 occupation of the frontier orbitals of both spins. For $\zeta = 0.32$, from the WPP calculations for the freestanding molecule we obtain the energy of the LUMO orbital, $E_{\text{LUMO}} = -3.19$ eV, with respect to the vacuum level in good agreement with the PTCDA affinity reported in Refs. [97,98]. We also obtain that the energies of unoccupied orbitals, $E_{\text{LUMO}+1} = -1.88$ eV and $E_{\text{LUMO}+2} = -1.85$ eV. The energy difference between LUMO+2 and LUMO is then close to the $D_1^- \rightarrow D_0^-$ spectral line of the PTCDA anion [80]. The configuration with empty LUMO orbital and singly occupied LUMO+2 can then be seen as representation of the D_1^- many-body state of PTCDA [80]. It is important to realize that the electron-

molecule interaction is determined such that it reproduces the many-body energies of the freestanding molecule. No parameter adjustment is performed *a posteriori* to fit the experimental or *ab initio* results for the molecule interacting with metal.

The change of the electron-metal interaction because of the presence of the molecule $\Delta V_S(\mathbf{r})$ is set as

$$\Delta V_S(\mathbf{r}) = \begin{cases} -V^L[x, y, -(z+d)], & z > 0 \\ 0, & z \leq 0. \end{cases} \quad (6)$$

This choice guarantees that at the image potential plane defined with $\mathbf{r} = (x, y, 0)$, the local part of the electron-molecule interaction is fully screened, $V^L + \Delta V_S = 0$. Since the nonlocal potential $V^{NL}(\mathbf{r})$ consists of very short-range contributions around the atoms within the molecule (the nonlocal potential range is smaller than the molecule-surface distance d), we also obtain that $V_M + \Delta V_S = 0$ at the image plane.

The electron-metal substrate interaction potential $V_S(z)$ is represented with an analytical model potential which is only a function of the electron coordinate z measured along the surface normal. The free-electron motion parallel to the surface is assumed. To address the role of the band structure of the substrate in RCT, we use two representations of the metal substrate. The first is given by the free-electron (jellium) model potential of Jennings *et al.* [99]:

$$V_S(z) = \begin{cases} -\frac{1}{4z}\{1 - e^{-\lambda z}\}, & z > 0 \\ \frac{U_0}{Ae^{Bz}+1} & \text{otherwise.} \end{cases} \quad (7)$$

It smoothly joins the constant potential U_0 inside the metal with $-1/4z$ image potential for an electron in vacuum. We use $U_0 = -12$ eV for the conduction-band bottom and parameter $\lambda = 1.171$ a.u., consistent with the Ag(111) model potential discussed below. Parameters A and $B > 0$ are obtained requiring continuity of potential and its derivative. The second representation of the metal substrate is given by the Ag(111) model potential (see Ref. [86] for an analytical expression and values of the parameters). It correctly reproduces the Ag(111) projected band structure at the $\bar{\Gamma}$ point; in particular, the projected band gap (L gap), where an electron cannot propagate inside metal in the z direction perpendicular to the surface within the energy range from -4.96 to -0.66 eV with respect to the vacuum level, and the bottom of the 2D surface-state continuum. Within the surface-state continuum, an electron is bound to the surface in z direction and propagates freely parallel to it. At the $\bar{\Gamma}$ point, the surface state is at -0.065 eV with respect to the Fermi level, i.e., at -4.625 eV with respect to the vacuum level considering the work function of Ag(111) of 4.56 eV [86]. In the past, both representations of the metal substrate were successively used in surface science to describe the excited electron dynamics at surfaces [10,100,101].

Finally, the absorbing potential $V_a(\mathbf{r})$ is introduced at the boundaries of the computational box, and it is zero in the ‘‘analysis’’ region inside the computational box. The analysis region is used for the extraction of the characteristics of the molecule-localized resonances. Developed in the context of the quantum WPP calculations of scattering and reaction dynamics [83,102–106], the absorbing potential allows one to impose the outgoing wave boundary conditions consistent

with calculation of the decaying molecule-localized states. Given the localization of the initial wave function, the electron wave function evolution inside the analysis region of the finite computational mesh is then equivalent to the wave-function evolution in the analysis region being part of the infinite space. We use the quadratic form of the absorbing potential. As an example, for the molecule oriented parallel to the free-electron metal surface, the mesh is symmetric in the x and y coordinates, with $-R \leq x \leq R$, $-R \leq y \leq R$. The mesh in the z coordinate is defined by $z_- \leq z \leq z_+$ (typically, we use $z_- = -84$ a.u., $z_+ = 30$ a.u., where the geometrical center of the molecule is at $x = y = 0$, $z = d$). The absorbing potential in this situation is given by

$$\begin{aligned} iV_a(\mathbf{r}) = & \chi \Theta[|x| - (R - L)][|x| - (R - L)]^2/L^2 \\ & + \chi \Theta[|y| - (R - L)][|y| - (R - L)]^2/L^2 \\ & + \chi_m \Theta[(z_- + L_m) - z][(z_- + L_m) - z]^2/L_m^2 \\ & + \chi_v \Theta[z - (z_+ - L_v)][z - (z_+ - L_v)]^2/L_v^2, \end{aligned} \quad (8)$$

where $\Theta(x)$ is the step function, $L = 15$ a.u. is the range of the absorption area in the x and y coordinates, $L_m = 50$ a.u. ($L_v = 10$ a.u.) is the metal (vacuum) range of the absorption area in the z coordinate, and the amplitudes $\chi = 0.2$ a.u., $\chi_m = 0.25$ a.u., and $\chi_v = 0.15$ a.u.

III. ELECTRON TRANSFER BETWEEN PTCDA MOLECULE AND METAL SUBSTRATE

A. Energies and electron transfer rates of the PTCDA molecule-localized resonances

In Fig. 2, we show the energies E_m and resonant charge transfer rates Γ_m or, equivalently, widths of the PTCDA molecule-localized resonances with $m = (\text{LUMO}, \text{LUMO} + 1, \text{LUMO} + 2)$ character. The molecule is placed in front of the metal surface at a distance d measured from the image plane. The molecular plane is parallel to the metal surface, as sketched in Fig. 1 for $\alpha = 0$. The WPP calculations are performed for d varying from ≈ 6 Å down to the adsorption distances d_{ads} . For the Ag(111) surface, it was found that PTCDA adsorbs at 2.9 Å from the surface layer of atoms [63,76,89,90,107], i.e., $d_{\text{ads}} \approx 3.3$ a.u. from the image plane. Here, we used $d_{\text{ads}} = 3.5$ a.u. Studying the distances $d > d_{\text{ads}}$ is of relevance for situations where the molecule is separated from the metal by the dielectric spacer layer(s), such as ionic crystals, which can be modeled by the vacuum gap of a given width [108].

We compare results of the WPP calculations performed using the jellium and Ag(111) [86] model potential description of the metal. While the free-electron model results provide general trends of the molecule coupling with metal, the band structure of the latter might significantly affect the RCT, as has been discussed for the case of atomic adsorbates at surfaces [10].

The energies of the LUMO, LUMO+1, and LUMO+2 resonances obtained with two descriptions of the metal [Fig. 2(a)] are very close to each other. Indeed, the shift of the resonant energies E_m with respect to the energies of the freestanding molecule orbitals, E_m^0 , can be roughly estimated from the perturbation theory as an external potential at the center of

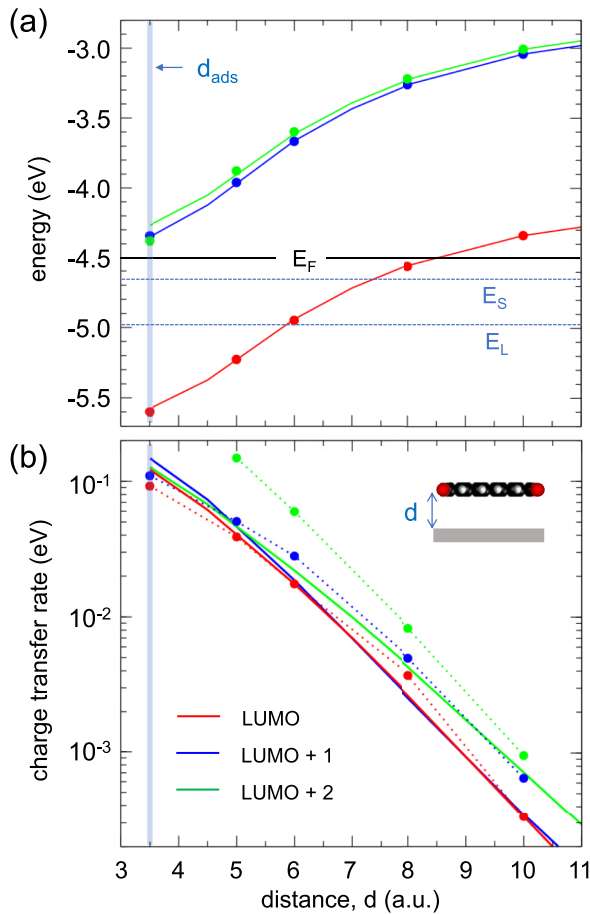


FIG. 2. PTCDA molecule in front of the metal surface. (a) Energies and (b) widths (RCT rates) of molecule-localized resonances with LUMO (red), LUMO+1 (blue), and LUMO+2 (green) character [see the inset of (b) for the color code]. The WPP results for the free-electron metal substrate are shown with solid lines, and the WPP results for the model Ag(111) substrate are shown with (a) circles and with (b) dashed lines with circles. The molecular plane is parallel to the metal surface, as sketched in the inset of (b). Results are shown as a function of the distance d between the molecular plane and image potential plane of the metal. The horizontal black line labeled as E_F in (a) indicates the Fermi level of the metal. Specific energies of the model Ag(111) surface are shown in (a) with horizontal blue lines: the surface-state energy at the $\bar{\Gamma}$ point is E_S , and the bottom of the projected L gap at the $\bar{\Gamma}$ point is E_L . The vertical blue line in both panels indicates the adsorption distance d_{ads} .

the molecule, $E_m \sim E_m^0 + \{V_S(d) + \Delta V_S[\mathbf{r} = (0, 0, d)]\}$. To a large extent, it is thus determined by the image part of the electron-metal interaction potential with $-1/4d$ dependence on d , which is the same for the free-electron and Ag(111) model potential description of the metal.

Recall that within the present approach, the many-body ground state of molecular anion PTCDA⁻ is mapped into the single-electron occupying LUMO, while its excited states are mapped into the single-electron occupying LUMO+1 or LUMO+2 orbitals. The downshift of the active orbital energy reflects an interaction of molecular anion with its electrostatic image created by the metal surface and leading to the higher electron detachment energy [76,89,109–112]. Close to the

surface, for $d < 8$ a.u., $E_{\text{LUMO}} < E_F$, i.e., the LUMO is at energy resonance with occupied electronic states of the metal. The LUMO+1 and LUMO+2 are at energy resonance with unoccupied electronic states above E_F .

In accord with earlier studies [61,76,95,97], we obtain that the molecule adsorbs as a negative ion with occupied LUMO resonance at 1 eV below the Fermi level for $d = d_{\text{ads}}$. The experimental and *ab initio* studies report $E_{\text{LUMO}} \approx 0.5$ eV below E_F [61,63,88,94,95,113]. Despite this discrepancy, the one-electron model performs reasonably well given its simplicity where the atomic rearrangements and complex electronic structure of the metal/molecule interface are not accounted for. Interestingly, a similar energy difference between E_{LUMO} and E_F has been reported for the PTCDA adsorption on spacer ionic crystal layers on metal [47,114]. This can be attributed to the high static dielectric constant of ionic crystals and thus image charge effects similar to that of metal (see, also, Ref. [38]).

The RCT rates Γ_m calculated with WPP [Fig. 2(b)] decrease exponentially with increasing d . The exponential decrease of the RCT rates when separating the molecule from the surface by a spacer layer (here, vacuum) reflects the decoupling of the molecule-localized electronic states from that of the metal substrate. This effect of the spacer allows one to reach sufficiently long lifetimes of molecule-localized electronic states so that the scanning probes can be utilized to manipulate charges of adsorbed species and to control atomic rearrangements and reactions [34–42], as well as to study the atomically resolved photon emission from unique molecules [43–49]. Interestingly, representing RCT rates in the form $\Gamma(d) = \gamma e^{-\sigma d}$, we obtain the exponential decay constant $\sigma \approx 2 \text{ \AA}^{-1}$ so that vacuum is a more efficient spacer than NaCl, where $\sigma \approx 1.1 \text{ \AA}^{-1}$ has been found experimentally for the H₂Pc molecule [33] (we considered that the width of the NaCl monolayer is 2.8 \AA [115–117]).

For the adsorption distance, and up to $d = 6$ a.u., E_{LUMO} is below the projected band gap of Ag(111) and it is close to the projected band-gap edge for larger d . In this situation, the RCT is only mildly affected by the metal band structure effects, as evidenced by the WPP results showing similar Γ_{LUMO} for both descriptions of the substrate [free-electron metal and Ag(111)]. For the molecule adsorbed on the Ag(111) surface we find that $\Gamma_{\text{LUMO}} = 92$ meV corresponding to the 7 fs electron transfer time between an adsorbate and the substrate. This is consistent with the experimental findings and *ab initio* calculations. Thus, $\Gamma_{\text{LUMO}} = 440$ meV was deduced using a vibrational frequency as a clock [118]; and $\Gamma_{\text{LUMO}} = 50$ – 125 meV can be obtained from the study of the Kondo effect reported in Ref. [70] using intraorbital Coulomb repulsion $U = 0.5$ – 1.0 eV calculated *ab initio* [62,63]. Moreover, the 200 meV broadening of the LUMO resonance measured experimentally and calculated *ab initio* has been reported by the Tautz group [63,88].

Interestingly, the RCT rates calculated for the LUMO+1 and LUMO+2 resonances are at odds with the common wisdom gained in studies of the RCT between atomic species and metal surfaces [10,119,120].

First, for the free-electron metal surface, the lower binding energies of the LUMO+1 and LUMO+2 orbitals as compared to LUMO lead to the (i) lower potential barrier for an electron

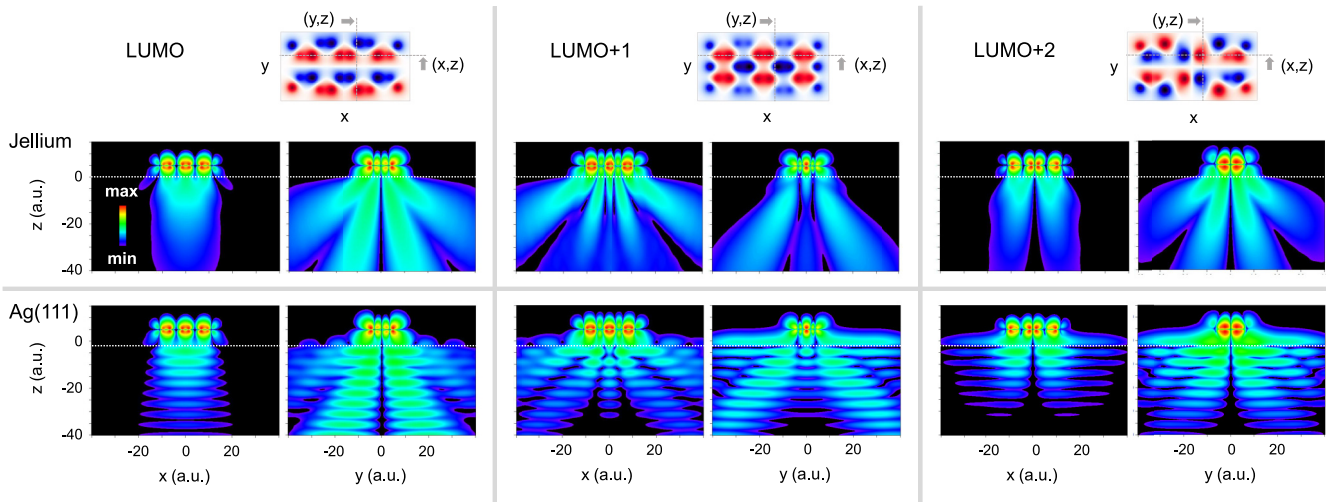


FIG. 3. Decaying resonances. Top row: Wave functions of LUMO, LUMO+1, and LUMO+2 orbitals of the freestanding PTCDA calculated with wave-packet propagation. Results are shown at 1 a.u. above the molecular plane to avoid the wave-function node of the π -electron system. The red (blue) color stands for the positive (negative) values. The dashed gray lines indicate the location of the (x, z) and (y, z) planes used below for the 2D maps of the probability density of the corresponding resonances for the molecule adsorbed on metal. Middle and bottom rows: Analysis of the decay of the PTCDA anion placed at $d = 5$ a.u. in front of the free-electron metal (jellium, middle row) and Ag(111) metal (bottom row). The geometrical center of the molecule is located at $(x = 0, y = 0, z = d)$. Interpolated 2D (x, z) and (y, z) maps of the probability density $\varrho_m(\mathbf{r}) = |\psi(\mathbf{r}, E_m)|^2$ calculated with WPP for the PTCDA-localized resonances with $m = (\text{LUMO}, \text{LUMO} + 1, \text{LUMO} + 2)$ character. The position of the analysis (x, z) and (y, z) planes is indicated in the top row. Results are shown in the logarithmic scale $\ln(\varrho_m)$ covering the $e^{-12} \rightarrow 1$ range of ϱ_m . The color code is explained in the inset of the leftmost panel of the jellium results. The white dotted horizontal line in all panels shows the position of the $(x, y, z = 0)$ image plane of the metal. The metal is at $z < 0$ and vacuum is at $z > 0$.

tunneling between the molecule and the metal, and (ii) larger spatial extension of their wave functions. One thus would expect that $\Gamma_{\text{LUMO}+1}$ and $\Gamma_{\text{LUMO}+2}$ are essentially larger than Γ_{LUMO} , and their exponential decrease with increasing d is slower [119,120]. However, this intuitive picture is not confirmed by the present WPP results that show $\Gamma_{\text{LUMO}} \approx \Gamma_{\text{LUMO}+1}$. It is only $\Gamma_{\text{LUMO}+2}$ that appears somewhat larger at $d \gtrsim 6$ a.u. and features a slower exponential decrease with d .

Second, for the Ag(111) model incorporating the projected band structure, the $E_{\text{LUMO}+1}$ and $E_{\text{LUMO}+2}$ are located within the L gap of the substrate. The corresponding propagating electronic states of the metal are removed from the adsorbate coupling with substrate, and the RCT in the direction perpendicular to the surface is not possible. Since this is the shortest and thus preferential direction of the RCT, one would expect that the RCT rates are reduced as compared to the free-electron metal surface. This tendency has been reported in a number of studies of atomic adsorbates on metal surfaces [10] (see, also, Refs. [73,74]). However, the results reported in Fig. 2(b) for the PTCDA anion clearly show different trends, with $E_{\text{LUMO}+1}$ and $E_{\text{LUMO}+2}$ larger for the model Ag(111) as compared to the free-electron metal.

In order to elucidate the orbital and substrate dependence of the RCT, we analyze the wave functions of molecule-localized resonances calculated with WPP.

B. Wave functions of the quasistationary molecular orbitals

The 2D maps of the wave functions of the PTCDA molecule-localized resonances are shown in Fig. 3. These states decay via an electron (LUMO+1, LUMO+2) or hole

(LUMO) transfer into the surface, which can be visualized from the associated probability density $\varrho_m(\mathbf{r}) = |\psi(\mathbf{r}, E_m)|^2$, where $m = (\text{LUMO}, \text{LUMO} + 1, \text{LUMO} + 2)$. The molecule is placed at $d = 5$ a.u. in front of the free-electron metal surface (middle row) and model Ag(111) surface (bottom row). Results are shown in the (x, z) and (y, z) planes perpendicular to the surface (see top row of panels for the positions of the analysis planes).

The number of features is common for both representations of the metal. Thus, the resonance wave functions in vacuum above the surface ($z > 0$) closely resemble the orbitals of the freestanding molecule. Inside the metal ($z < 0$), the probability density reflects the outgoing electron (or hole) flux leaking into the metal bulk because of the population decay of the molecule-localized state. The symmetry and the structure of the molecular orbitals imposes the gross pattern of the decay. For example, even though the adsorbate/substrate coupling is typically strongest along the direction perpendicular to the surface corresponding to the lowest potential barrier between the two, there is no outgoing probability flux along the z axis for the resonances with LUMO and LUMO+2 character. This is because their wave functions are antisymmetric with respect to $y \rightarrow -y$ (LUMO) or $x \rightarrow -x$ and $y \rightarrow -y$ (LUMO+2) transformations. Similarly, one observes that along with symmetry constraints, the RCT for the free-electron metal and Ag(111) involves preferentially electronic states of the metal continuum propagating in certain directions.

This latter finding can be explained using the perturbation theory for rearranging collisions [121,122] and considering the translational symmetry of the model metal potentials in a direction parallel to the surface. The coupling matrix

elements $V_m(k_{\parallel})$ between molecular-orbital $\psi_m(\mathbf{r})$ and metal states $\Phi(\mathbf{r}, \mathbf{k}_{\parallel}, E_m) = \phi(z, E_{\perp}) \exp(i\mathbf{r}_{\parallel} \mathbf{k}_{\parallel})$ can be found from $V_m(k_{\parallel}) = \iint \phi^*(z, E_{\perp}) \exp(-i\mathbf{r}_{\parallel} \mathbf{k}_{\parallel}) V_S(z) \psi_m(\mathbf{r}) d^3\mathbf{r}$, where $\mathbf{r}_{\parallel}(\mathbf{k}_{\parallel})$ is the radius vector (momentum) parallel to the surface and $E_m = E_{\perp} + k_{\parallel}^2/2$. Thus, $V_m(k_{\parallel})$ depends on the 2D Fourier transform of the molecular orbital, which results in the multiray structure of the outgoing probability flux. Similar conclusions can be obtained from the Bardeen theory of electron tunneling [73,74].

The symmetry and the complex structure of the coupling between molecule-localized electronic states and those of the metal continuum affect an efficiency of the RCT. Thus, the LUMO+1 resonance has essentially lower binding energy than LUMO resonance, and therefore the barrier for electron tunneling from LUMO+1 to the metal is, overall, lower so that the RCT should be faster. However, the decay of the LUMO orbital involves metal continuum states with smaller electron momentum along the x axis k_x , i.e., electrons can be transferred closer to perpendicular to the surface direction, which increases the efficiency of the RCT [compare the (x, z) maps of LUMO and LUMO+1 resonances in Fig. 3]. As a net result, for the free-electron metal, this finally leads to $\Gamma_{\text{LUMO}} \approx \Gamma_{\text{LUMO}+1}$ (see Fig. 2). For the Ag(111) surface, $\Gamma_{\text{LUMO}} < \Gamma_{\text{LUMO}+1}$ which reflects the role of the metal band structure and, in particular, of the decay into the 2D surface-state continuum, discussed below.

Along with features common for the free-electron and Ag(111) surfaces, it follows from the WPP results in Fig. 3 that the band structure of the metal produces apparent as well as more subtle differences in the decay. Thus, the oscillations in $q_m(\mathbf{r})$ inside Ag(111) reflect the periodic arrangement of the atomic planes parallel to the surface. As we already pointed out, for molecule-localized states with energies inside the projected band gap of Ag(111), the RCT along the surface normal is not possible. The outgoing flux can only exist at a finite angle from this direction [10,73,74], similarly to the situation imposed by the symmetry. The band structure effect is absent for the LUMO resonance with energy below the L gap. For the LUMO+1 orbital and for the (x, z) map for the LUMO+2 orbital, a careful comparison of the probability density inside the free-electron metal and Ag(111) shows that for Ag(111), the decay along the surface normal is suppressed. For the (y, z) map of the LUMO+2 resonance, this effect is masked by the symmetry constraints. Observe that despite the removal of some efficient decay channels, the RCT rates of the resonances with LUMO+1 and LUMO+2 character shown in Fig. 2(b) are larger for Ag(111) and smaller for the free-electron metal, as we pointed out before.

This is because for the molecule placed in front of the Ag(111) surface, there is an additional efficient RCT channel associated with resonance population decay into the 2D surface-state continuum [10,74]. The 2D surface-state continuum of the (111) surfaces of noble metals corresponds to the electronic states propagating parallel to the surface. The energy dispersion of the surface continuum states is given by $E_{2D}(\mathbf{k}_{\parallel}) = E_S + k_{\parallel}^2/2$. For the molecule-localized resonances with energies $E_m > E_S$, which is the case for LUMO+1 and LUMO+2, this decay channel involves the electronic states of the surface-state continuum with $k_{\parallel} = \sqrt{2(E_m - E_S)}$. It manifests itself as probability density flux propagating

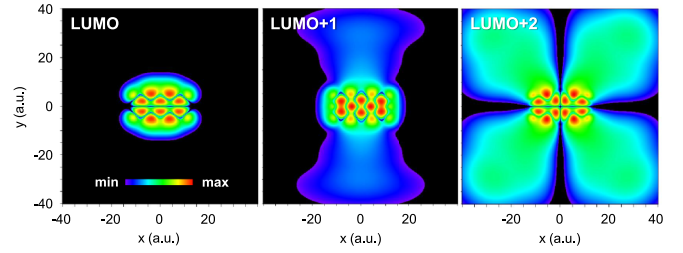


FIG. 4. Role of the surface-state continuum in RCT. The panels of the figure show interpolated 2D maps of the probability density $q_m(x, y, z = 0) = |\psi(x, y, z = 0, E_m)|^2$ calculated within the image plane of the metal for the PTCDA-localized resonances with $m = (\text{LUMO}, \text{LUMO} + 1, \text{LUMO} + 2)$ character. The molecule is at $d = 5$ a.u. above the surface. Results are shown in the logarithmic scale covering the $e^{-10} \rightarrow 1$ range. The color code is explained in the insert.

parallel to the metal surface with maximum close to the position of the image plane ($z = 0$, white dashed line) which is apparent in the (y, z) (LUMO+1) and (x, z) , and (y, z) (LUMO+2) maps in the bottom row of Fig. 3. The energy of the LUMO resonance is below the surface-state continuum for the molecule-surface distances below $d = 6$ a.u. so that this RCT channel is closed.

The decay of the molecule-localized resonances into the 2D continuum of states propagating along the metal surface is further confirmed in Fig. 4, which shows the probability density of resonant wave functions $|\psi(x, y, z = 0, E_m)|^2$ calculated within the image plane of the metal. The PTCDA molecule is placed at $d = 5$ a.u. in front of the Ag(111) surface. While no outgoing probability flux is seen for the LUMO resonance, the LUMO+1 resonance features directional decay along y . Similarly to the above discussion of the decay into the 3D metal bulk continuum, the directionality of the decay into the 2D surface-state continuum stems from the \mathbf{k}_{\parallel} dependence of the coupling matrix elements between molecular orbital $\psi_m(\mathbf{r})$ and electronic states of the 2D surface-state continuum $\phi_S(z, E_S) \exp(i\mathbf{r}_{\parallel} \mathbf{k}_{\parallel})$, where $E_m = E_S + k_{\parallel}^2/2$, and $\phi_S(z, E_S)$ is the bound state wave function of the surface state at the $\bar{\Gamma}$ point ($k_{\parallel} = 0$). The LUMO+2 resonance has the strongest coupling with the surface-state continuum and features an intense four-lobe decay pattern constrained by the orbital symmetry. This is consistent with the strongest increase of the RCT rate, $\Gamma_{\text{LUMO}+2}$, as compared to the free-electron metal [see Fig. 2(b)].

C. Controlling molecule-surface coupling with STM manipulation

Controlling the lifetimes of molecule-localized resonances can be achieved not only varying the molecule-surface distance with spacer layers, but also changing the adsorption geometry. We consider here an evolution of the PTCDA-molecule/Ag(111)-metal interaction during the STM manipulation. As has been thoroughly studied experimentally and using *ab initio* approaches [62,63,69,70], when the STM tip contacts one of the carboxylic oxygen atoms of PTCDA, a bond is formed. Upon retracting the tip, the molecule is lifted up, while keeping the contact with the substrate at the

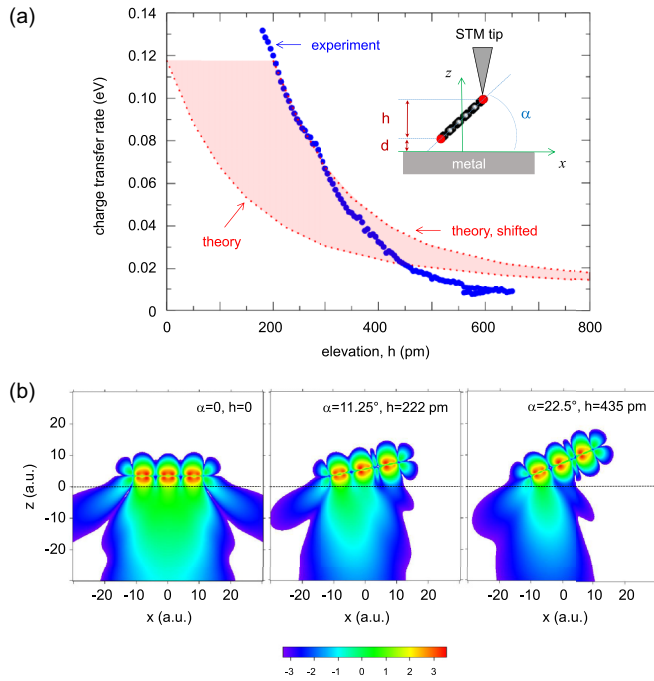


FIG. 5. Evolution of the coupling between the LUMO orbital of the PTCDA anion and free-electron metal upon molecular manipulation with STM sketched in the inset of (a). (a) Charge transfer rate Γ_{LUMO} as a function of molecular elevation h . Blue dots: experimental data from Ref. [70] obtained assuming the intraorbital Coulomb repulsion $U = 1.0$ eV. The WPP results are shown with a red dashed line marked “theory”. Red dashed line marked “theory, shifted” shows the WPP data, where the elevation h has been offset by +200 pm to account for the difference between the simplified geometry considered here and a realistic molecular deformation upon elevation [62,63]. The hatched area shows the theoretical uncertainty because of the model geometry. For further details, see the text. (b) The interpolated 2D (x, z) maps of the probability density of the molecule-localized resonance with LUMO character (see Fig. 3 for the definition of the analysis plane). The $\ln[|\psi(x, y_0, z, E_{\text{LUMO}})|^2]$ ($y_0 = 1$ a.u.) is shown as a function of the x and z coordinates for molecular elevation $h = 0$, $h = 222$ pm, and $h = 435$ pm. For $h = 0$, the molecule is at $d = 5$ a.u. above the surface. The color code is explained in the inset. The black horizontal line shows the position of the $(x, y, z = 0)$ image plane of the metal. The origin of the abscissa axis $x = 0$ corresponds to the geometrical center of the molecule located parallel to the surface ($h = 0$). The metal is at $z < 0$ and vacuum is at $z > 0$.

opposite end. This situation is schematically sketched in the inset of Fig. 5(a) and in Fig. 1(b). The large mechanical tunability of the system has been used to address the Kondo regime [62,63,69,70]. In addition, the RCT rate between the LUMO resonance and Ag(111) substrate has been experimentally found to vary by an order of magnitude upon molecular lift up [70].

To study to which extent the above experimental finding can be addressed using a simple model, we applied the WPP approach considering that the flat rigid molecule rotates around the axis formed by the carboxylic oxygens opposed to the STM tip [see Fig. 1(b)]. In reality, the molecule experiences torsion and bending deformations that have been

demonstrated *ab initio* [62,63]. Since the RCT rates between the molecule and the tip are essentially smaller than those between the molecule and the metal [70], we neglected the interaction between an active electron and the tip. As a further simplification, given that the RCT rates between the LUMO resonance and metal substrate are nearly independent of the projected band structure (see Fig. 2), we used the free-electron representation of the metal, allowing us to further reduce the numerical effort.

The calculated evolution of the RCT rate Γ_{LUMO} upon molecular lift up is reported in Fig. 5(a). The WPP results are compared with the experimental data from Ref. [70], where the molecule-surface coupling strength was deduced from an analysis of the Kondo temperature and conductance of the junction. The present approach reproduces the experimentally determined Γ_{LUMO} for the molecule adsorbed on a metal surface ($h = 0$), as has already been discussed above. For molecular elevation h within the 600–800 pm range, the calculated RCT coupling drops by an order of magnitude and basically reaches the limit of the vertical upright geometry where the molecule is positioned vertically perpendicular to the surface ($h \approx 1000$ pm). In this latter situation, in agreement with experiment, we find $\Gamma_{\text{LUMO}} = 9$ meV, i.e., ≈ 72 fs timescale for the RCT. We obtain a similar (an order of magnitude) reduction of $\Gamma_{\text{LUMO}+1}$ and $\Gamma_{\text{LUMO}+2}$ for the change of the adsorption geometry from parallel to perpendicular to the surface. In Fig. 5(b), we show the interpolated 2D (x, z) maps of the probability density of the molecule-localized resonance with LUMO character calculated for different values of elevation h . The modification of the wave function inside metal with increasing h illustrates the adsorbate decoupling from the substrate upon changing the adsorption geometry from a flat to upright standing molecule. Primarily, this is reflected in an overall reduction of the probability flux leaving the molecule-localized state.

While the experimentally determined RCT rates are reproduced at two extreme points of molecular manipulation, there is an essential difference between experiment and theory in the intermediate- h range. Indeed, Γ_{LUMO} calculated with WPP decreases immediately as soon as h is increased. In the experimental data, the variation of the properties of the LUMO resonance is delayed [63,70]. This is a direct consequence of the PTCDA deformation not accounted for in the present study. Because of the bending and torsion of the molecule, the oxygen from the second carboxyl group starts to lift up and follow the tip only for $h > 200$ pm, as has been demonstrated *ab initio* [63]. The red dashed line marked “theory, shifted” shows the WPP data, where the elevation h has been offset by +200 pm to account for this effect. Obviously, an agreement between experiment and theory is improved. However, this is an upper estimate of the effect of the molecular deformation since an average molecular elevation will be between the limits given by the two dashed lines in Fig. 5(a).

Before closing this section, we would like to point out that reduction of the RCT rates for the molecule standing upright at the surface is of importance for molecular fluorescence in plasmonic junctions. Recently, the interplay of radiative and RCT decay channels of the excited state population has been addressed theoretically for molecular chromophores adsorbed on a metal surface, and a metal surface with a spacer layer

TABLE I. Properties of the resonance with LUMO character for the PTCDA molecule adsorbed on the Ag(111) surface (parallel geometry) or lifted up perpendicular to the metal surface by an STM manipulation. Binding energy refers to the Fermi level assuming the work function of Ag(111) surface of 4.56 eV [86]. The WPP results are compared with experimental data and *ab initio* calculations. For Ref. [70], Γ_{LUMO} can be obtained using intraorbital Coulomb repulsion $U = 0.5\text{--}1.0$ eV calculated *ab initio* [62,63].

	Binding energy, parallel E_{LUMO} (meV)	Width, parallel Γ_{LUMO} (eV)	Width, perpendicular Γ_{LUMO} (eV)
Experiment, <i>ab initio</i>	300–500 [61,63,88,94,95,113]	65–131 [70], 200 [63,88], 440 [118]	4.5–9 [70]
Present WPP	1030	92	9

of ionic crystal within a gap of plasmonic antenna [108]. The RCT rates within the 10 meV range as obtained here for the molecule oriented perpendicular to the surface should allow one to observe molecular fluorescence [108]. This is while the molecule is in direct contact with metal. For the molecule adsorbed on a metal in a flat geometry, the photon emission is impossible without the spacer layer [24,28,30,42].

IV. SUMMARY, CONCLUSIONS, AND OUTLOOK

In conclusion, using the model one-electron description and WPP approach, we have studied the electron transfer between the PTCDA molecule and metal surface represented as the free-electron metal or as Ag(111). For the situation where the PTCDA molecule is adsorbed on the Ag(111) substrate, the WPP results for the energy and width of the molecular resonance with LUMO character are in semiquantitative agreement with experiment and *ab initio* theory, as summarized in Table I. This shows that our approach is well suited for the present system and allows us to confidently discuss an essential robust physics of the RCT that it reveals.

(i) Analysis of the energies, widths, and resonance wave functions of molecular orbitals with π character calculated as a function of the distance between the PTCDA molecule and the metal shows that the molecular symmetry and projected band structure of the substrate play a decisive role in determining electron transfer in the system.

(ii) For the planar molecule as PTCDA, the RCT rates between the molecule and the surface are reduced by an order of magnitude when the adsorption geometry is changed from the flat to standing upright. This reflects the possibility to geometrically tune the adsorbate/substrate coupling with possible application to tunneling or light-emitting devices.

(iii) The resonances with LUMO+1 and LUMO+2 character representing excited states of molecular anion and located within the projected band gap of Ag(111) strongly interact with the 2D surface-state continuum. The corresponding

excited electron is not injected from the molecule into the metal bulk, but moves, for a certain time, parallel to the surface. It will thus experience confinement within surface kagome structures or quantum corrals. This opens further possibility to tune the lifetimes of excited states.

We also addressed the STM manipulation as a means to control the lifetimes of molecule-localized states. The PTCDA molecule initially adsorbed on Ag(111) in a flat geometry is lifted up perpendicular to the surface. While agreement with experiment is reached at extreme points of this manipulation with an order of magnitude reduction of the RCT for the upright standing geometry, the evolution of molecule/surface coupling along the entire manipulation path is purely reproduced. This indicates an essential role of molecular deformation not included in the present study.

We believe that along with analysis of various aspects of the RCT, the present work shows an interest in model approaches providing a semiquantitative description of the RCT between organic chromophores and metal surfaces at moderate computational cost. The capacity to estimate the RCT efficiency is of paramount importance for designing novel experiments to address many processes at surfaces such as surface reactivity, light emission, or photoexcitation and photoemission induced by intense and short optical pulses interacting with an adsorbate. In the latter case, the WPP offers a direct time-domain access to the system dynamics.

ACKNOWLEDGMENTS

The author gratefully acknowledges the warm hospitality of DIPC and fruitful discussions with T. Neuman, J. Aizpurua, G. Schull, and E. L. Moal. The author gratefully acknowledges M. Žonda and M. Švec for providing the experimental data for Fig. 5. This work has been supported by the “Investissements d’Avenir” LabEx PALM (Grant No. ANR-10-LABX-0039-PALM).

[1] J. W. Gadzuk, *Phys. Rev. B* **1**, 2110 (1970).
 [2] P. Nordlander and J. C. Tully, *Phys. Rev. B* **42**, 5564 (1990).
 [3] J. Los and J. Geerlings, *Phys. Rep.* **190**, 133 (1990).
 [4] H. Winter, *Phys. Rep.* **367**, 387 (2002).
 [5] J. W. Gadzuk and J. K. Norskov, *J. Chem. Phys.* **81**, 2828 (1984).
 [6] H. Nienhaus, *Surf. Sci. Rep.* **45**, 1 (2002).

[7] R. Palmer, *Prog. Surf. Sci.* **41**, 51 (1992).
 [8] M. Bauer, S. Pawlik, and M. Aeschlimann, *Phys. Rev. B* **55**, 10040 (1997).
 [9] H. Petek, M. J. Weida, H. Nagano, and S. Ogawa, *Science* **288**, 1402 (2000).
 [10] E. V. Chulkov, A. G. Borisov, J. P. Gauyacq, D. Sánchez-Portal, V. M. Silkin, V. P. Zhukov, and P. M. Echenique, *Chem. Rev.* **106**, 4160 (2006).

- [11] C. D. Lindstrom and X.-Y. Zhu, *Chem. Rev.* **106**, 4281 (2006).
- [12] J. Gavnholt, T. Olsen, M. Englund, and J. Schiøtz, *Phys. Rev. B* **78**, 075441 (2008).
- [13] R. D. Muiño, D. Sánchez-Portal, V. M. Silkin, E. V. Chulkov, and P. M. Echenique, *Proc. Natl. Acad. Sci. USA* **108**, 971 (2011).
- [14] J. Gadzuk, *Surf. Sci.* **342**, 345 (1995).
- [15] P. Peumans, A. Yakimov, and S. R. Forrest, *J. Appl. Phys.* **93**, 3693 (2003).
- [16] S.-W. Hla and K.-H. Rieder, *Annu. Rev. Phys. Chem.* **54**, 307 (2003).
- [17] S. Günes, H. Neugebauer, and N. S. Sariciftci, *Chem. Rev.* **107**, 1324 (2007).
- [18] S. J. van der Molen, J. Liao, T. Kudernac, J. S. Agustsson, L. Bernard, M. Calame, B. J. van Wees, B. L. Feringa, and C. Schönenberger, *Nano Lett.* **9**, 76 (2009).
- [19] M. Galperin and A. Nitzan, *Phys. Chem. Chem. Phys.* **14**, 9421 (2012).
- [20] C. Große, P. Merino, A. Rosławska, O. Gunnarsson, K. Kuhnke, and K. Kern, *ACS Nano* **11**, 1230 (2017).
- [21] P. Avouris and R. E. Walkup, *Annu. Rev. Phys. Chem.* **40**, 173 (1989).
- [22] P. Saalfrank, *Curr. Opin. Solid State Mater. Sci.* **8**, 334 (2004).
- [23] P. Avouris and B. N. J. Persson, *J. Phys. Chem.* **88**, 837 (1984).
- [24] F. Rossel, M. Pivetta, and W.-D. Schneider, *Surf. Sci. Rep.* **65**, 129 (2010).
- [25] W. Gebauer, A. Langner, M. Schneider, M. Sokolowski, and E. Umbach, *Phys. Rev. B* **69**, 155431 (2004).
- [26] K. R. Rusimova, R. M. Purkiss, R. Howes, F. Lee, S. Crampin, and P. A. Sloan, *Science* **361**, 1012 (2018).
- [27] C. Brülke, O. Bauer, and M. M. Sokolowski, *Beilstein J. Nanotechnol.* **11**, 1663 (2020).
- [28] C. Zhang, L. Chen, R. Zhang, and Z. Dong, *Jpn. J. Appl. Phys.* **54**, 08LA01 (2015).
- [29] F. Schulz, M. Ijäs, R. Drost, S. K. Hämäläinen, A. Harju, A. P. Seitsonen, and P. Liljeroth, *Nat. Phys.* **11**, 229 (2015).
- [30] K. Kuhnke, C. Große, P. Merino, and K. Kern, *Chem. Rev.* **117**, 5174 (2017).
- [31] S. Kosłowski, D. Rosenblatt, A. Kabakchiev, K. Kuhnke, K. Kern, and U. Schlickum, *Beilstein J. Nanotechnol.* **8**, 1388 (2017).
- [32] S. Fatayer, F. Albrecht, I. Tavernelli, M. Persson, N. Moll, and L. Gross, *Phys. Rev. Lett.* **126**, 176801 (2021).
- [33] K. Kaiser, L.-A. Lieske, J. Repp, and L. Gross, *Nat. Commun.* **14**, 4988 (2023).
- [34] G. Mikaelian, N. Ogawa, X. W. Tu, and W. Ho, *J. Chem. Phys.* **124**, 131101 (2006).
- [35] L. Gross, *Nat. Chem.* **3**, 273 (2011).
- [36] T. Leoni, O. Guillermet, H. Walch, V. Langlais, A. Scheuermann, J. Bonvoisin, and S. Gauthier, *Phys. Rev. Lett.* **106**, 216103 (2011).
- [37] T. L. Cocker, D. Peller, P. Yu, J. Repp, and R. Huber, *Nature (London)* **539**, 263 (2016).
- [38] S. Fatayer, B. Schuler, W. Steurer, I. Scivetti, J. Repp, L. Gross, M. Persson, and G. Meyer, *Nat. Nanotechnol.* **13**, 376 (2018).
- [39] J. Doležal, P. Merino, J. Redondo, L. Ondič, A. Cahlík, and M. Švec, *Nano Lett.* **19**, 8605 (2019).
- [40] J. Doležal, P. Mutombo, D. Nachtigallová, P. Jelínek, P. Merino, and M. Švec, *ACS Nano* **14**, 8931 (2020).
- [41] D. Peller, L. Z. Kastner, T. Buchner, C. Roelcke, F. Albrecht, N. Moll, R. Huber, and J. Repp, *Nature (London)* **585**, 58 (2020).
- [42] B. Doppagne, T. Neuman, R. Soria-Martinez, L. E. P. López, H. Bulou, M. Romeo, S. Berciaud, F. Scheurer, J. Aizpurua, and G. Schull, *Nat. Nanotechnol.* **15**, 207 (2020).
- [43] Z. C. Dong, X. L. Zhang, H. Y. Gao, Y. Luo, C. Zhang, L. G. Chen, R. Zhang, X. Tao, Y. Zhang, J. L. Yang, and J. G. Hou, *Nat. Photon.* **4**, 50 (2010).
- [44] L. Zhang, Y.-J. Yu, L.-G. Chen, Y. Luo, B. Yang, F.-F. Kong, G. Chen, Y. Zhang, Q. Zhang, Y. Luo, J.-L. Yang, Z.-C. Dong, and J. G. Hou, *Nat. Commun.* **8**, 580 (2017).
- [45] H. Imada, K. Miwa, M. Imai-Imada, S. Kawahara, K. Kimura, and Y. Kim, *Nature (London)* **538**, 364 (2016).
- [46] G. Chen, Y. Luo, H. Gao, J. Jiang, Y. Yu, L. Zhang, Y. Zhang, X. Li, Z. Zhang, and Z. Dong, *Phys. Rev. Lett.* **122**, 177401 (2019).
- [47] K. Kimura, K. Miwa, H. Imada, M. Imai-Imada, S. Kawahara, J. Takeya, M. Kawai, M. Galperin, and Y. Kim, *Nature (London)* **570**, 210 (2019).
- [48] H. Imada, M. Imai-Imada, K. Miwa, H. Yamane, T. Iwasa, Y. Tanaka, N. Toriumi, K. Kimura, N. Yokoshi, A. Muranaka, M. Uchiyama, T. Taketsugu, Y. K. Kato, H. Ishihara, and Y. Kim, *Science* **373**, 95 (2021).
- [49] B. Doppagne, M. C. Chong, E. Lorchat, S. Berciaud, M. Romeo, H. Bulou, A. Boeglin, F. Scheurer, and G. Schull, *Phys. Rev. Lett.* **118**, 127401 (2017).
- [50] B. Yang, G. Chen, A. Ghafoor, Y. Zhang, Y. Zhang, Y. Zhang, Y. Luo, J. Yang, V. Sandoghdar, J. Aizpurua, Z. Dong, and J. G. Hou, *Nat. Photon.* **14**, 693 (2020).
- [51] A. Rosławska, T. c. v. Neuman, B. Doppagne, A. G. Borisov, M. Romeo, F. Scheurer, J. Aizpurua, and G. Schull, *Phys. Rev. X* **12**, 011012 (2022).
- [52] S. Jiang, T. Neuman, R. Bretel, A. Boeglin, F. Scheurer, E. Le Moal, and G. Schull, *Phys. Rev. Lett.* **130**, 126202 (2023).
- [53] S.-E. Zhu, Y.-M. Kuang, F. Geng, J.-Z. Zhu, C.-Z. Wang, Y.-J. Yu, Y. Luo, Y. Xiao, K.-Q. Liu, Q.-S. Meng, L. Zhang, S. Jiang, Y. Zhang, G.-W. Wang, Z.-C. Dong, and J. G. Hou, *J. Am. Chem. Soc.* **135**, 15794 (2013).
- [54] T. Esat, N. Friedrich, F. S. Tautz, and R. Temirov, *Nature (London)* **558**, 573 (2018).
- [55] C. Wagner, M. F. B. Green, P. Leinen, T. Deilmann, P. Krüger, M. Rohlfing, R. Temirov, and F. S. Tautz, *Phys. Rev. Lett.* **115**, 026101 (2015).
- [56] G. Reecht, F. Scheurer, V. Speisser, Y. J. Dappe, F. Mathevet, and G. Schull, *Phys. Rev. Lett.* **112**, 047403 (2014).
- [57] F. Evers, R. Korytár, S. Tewari, and J. M. van Ruitenbeek, *Rev. Mod. Phys.* **92**, 035001 (2020).
- [58] D. Sánchez-Portal, D. Menzel, and P. M. Echenique, *Phys. Rev. B* **76**, 235406 (2007).
- [59] A. Ravikumar, G. Kladnik, M. Müller, A. Cossaro, G. Bavdek, L. L. Patera, D. Sánchez-Portal, L. Venkataraman, A. Morgante, G. P. Brivio, D. Cvetko, and G. Fratesi, *Nanoscale* **10**, 8014 (2018).
- [60] R. J. Maurer and K. Reuter, *Angew. Chem. Intl. Ed.* **51**, 12009 (2012).
- [61] L. Romaner, D. Nabok, P. Puschnig, E. Zojer, and C. Ambrosch-Draxl, *New J. Phys.* **11**, 053010 (2009).

- [62] A. Greuling, M. Rohlfing, R. Temirov, F. S. Tautz, and F. B. Anders, *Phys. Rev. B* **84**, 125413 (2011).
- [63] A. Greuling, R. Temirov, B. Lechtenberg, F. B. Anders, M. Rohlfing, and F. S. Tautz, *Phys. Stat. Sol. (B)* **250**, 2386 (2013).
- [64] N. Papior, N. Lorente, T. Frederiksen, A. García, and M. Brandbyge, *Comput. Phys. Commun.* **212**, 8 (2017).
- [65] T. Frederiksen, M. Paulsson, M. Brandbyge, and A.-P. Jauho, *Phys. Rev. B* **75**, 205413 (2007).
- [66] M. Galperin and A. Nitzan, *J. Chem. Phys.* **124**, 234709 (2006).
- [67] K. Miwa, H. Imada, M. Imai-Imada, K. Kimura, M. Galperin, and Y. Kim, *Nano Lett.* **19**, 2803 (2019).
- [68] N. Lorente and M. Persson, *Phys. Rev. Lett.* **85**, 2997 (2000).
- [69] R. Temirov, A. Lassise, F. B. Anders, and F. S. Tautz, *Nanotechnology* **19**, 065401 (2008).
- [70] M. Žonda, O. Stetsovych, R. Korytár, M. Ternes, R. Temirov, A. Raccanelli, F. S. Tautz, P. Jelínek, T. Novotný, and M. Švec, *J. Phys. Chem. Lett.* **12**, 6320 (2021).
- [71] M. Plihal, D. C. Langreth, and P. Nordlander, *Phys. Rev. B* **59**, 13322 (1999).
- [72] A. G. Borisov, D. Teillet-Billy, J. P. Gauyacq, J. A. M. C. Silva, A. Mertens, C. Auth, and H. Winter, *Phys. Rev. B* **59**, 8218 (1999).
- [73] F. Aguilar-Galindo, A. G. Borisov, and S. Díaz-Tendero, *J. Chem. Theory Comput.* **17**, 639 (2021).
- [74] F. Aguilar-Galindo, A. G. Borisov, and S. Díaz-Tendero, *Appl. Surf. Sci.* **554**, 149311 (2021).
- [75] N. Friedrich, A. Roslowska, X. Arrieta, M. Romeo, E. L. Moal, F. Scheurer, J. Aizpurua, A. G. Borisov, T. Neuman, and G. Schull, [arXiv:2311.16805](https://arxiv.org/abs/2311.16805).
- [76] F. Tautz, *Prog. Surf. Sci.* **82**, 479 (2007).
- [77] M. Marks, A. Schöll, and U. Hüfer, *J. Electron Spectrosc. Relat. Phenom.* **195**, 263 (2014).
- [78] R. Otero, A. Vázquez de Parga, and J. Gallego, *Surf. Sci. Rep.* **72**, 105 (2017).
- [79] K. Stallberg, A. Namgalies, S. Chatterjee, and U. Höfer, *J. Phys. Chem. C* **126**, 12728 (2022).
- [80] J. Doležal, S. Canola, P. Hapala, R. C. de Campos Ferreira, P. Merino, and M. Švec, *ACS Nano* **16**, 1082 (2022).
- [81] M. Feit, J. Fleck, and A. Steiger, *J. Comput. Phys.* **47**, 412 (1982).
- [82] C. Leforestier, R. Bisseling, C. Cerjan, M. Feit, R. Friesner, A. Guldberg, A. Hammerich, G. Jolicard, W. Karrlein, H.-D. Meyer, N. Lipkin, O. Roncero, and R. Kosloff, *J. Comput. Phys.* **94**, 59 (1991).
- [83] D. Kosloff and R. Kosloff, *J. Comput. Phys.* **52**, 35 (1983).
- [84] C. C. Marston and G. G. Balint-Kurti, *J. Chem. Phys.* **91**, 3571 (1989).
- [85] R. Kosloff, The Fourier method, in *Numerical Grid Methods and Their Application to Schrödinger's Equation*, edited by C. Cerjan (Springer Netherlands, Dordrecht, 1993), pp. 175–194.
- [86] E. V. Chulkov, V. M. Silkin, and P. M. Echenique, *Surf. Sci.* **437**, 330 (1999).
- [87] P. Linstrom and W. Mallard, *NIST Chemistry WebBook, NIST Standard Reference Database No. 69* (National Institute of Standards and Technology, Gaithersburg, MD, 2023).
- [88] M. Rohlfing, R. Temirov, and F. S. Tautz, *Phys. Rev. B* **76**, 115421 (2007).
- [89] A. Hauschild, R. Temirov, S. Soubatch, O. Bauer, A. Schöll, B. C. C. Cowie, T.-L. Lee, F. S. Tautz, and M. Sokolowski, *Phys. Rev. B* **81**, 125432 (2010).
- [90] V. G. Ruiz, W. Liu, and A. Tkatchenko, *Phys. Rev. B* **93**, 035118 (2016).
- [91] J. P. Perdew and Y. Wang, *Phys. Rev. B* **45**, 13244 (1992).
- [92] X. Gonze, J.-M. Beuken, R. Caracas, F. Detraux, M. Fuchs, G.-M. Rignanese, L. Sindic, M. Verstraete, G. Zerah, F. Jollet, M. Torrent, A. Roy, M. Mikami, P. Ghosez, J.-Y. Raty, and D. Allan, *Comput. Mater. Sci.* **25**, 478 (2002).
- [93] L. Kleinman and D. M. Bylander, *Phys. Rev. Lett.* **48**, 1425 (1982).
- [94] A. Kraft, R. Temirov, S. K. M. Henze, S. Soubatch, M. Rohlfing, and F. S. Tautz, *Phys. Rev. B* **74**, 041402(R) (2006).
- [95] Y. Zou, L. Kilian, A. Schöll, T. Schmidt, R. Fink, and E. Umbach, *Surf. Sci.* **600**, 1240 (2006).
- [96] T. Koopmans, *Physica* **1**, 104 (1934).
- [97] O. T. Hofmann, V. Atalla, N. Moll, P. Rinke, and M. Scheffler, *New J. Phys.* **15**, 123028 (2013).
- [98] H. Sun, S. Ryno, C. Zhong, M. K. Ravva, Z. Sun, T. Körzdörfer, and J.-L. Brédas, *J. Chem. Theory Comput.* **12**, 2906 (2016).
- [99] P. J. Jennings, R. O. Jones, and M. Weinert, *Phys. Rev. B* **37**, 6113 (1988).
- [100] J. Kliewer, R. Berndt, E. V. Chulkov, V. M. Silkin, P. M. Echenique, and S. Crampin, *Science* **288**, 1399 (2000).
- [101] P. Echenique, R. Berndt, E. Chulkov, T. Fauster, A. Goldmann, and U. Höfer, *Surf. Sci. Rep.* **52**, 219 (2004).
- [102] T. Seideman and W. H. Miller, *J. Chem. Phys.* **96**, 4412 (1992).
- [103] U. V. Riss and H.-D. Meyer, *J. Phys. B: At. Mol. Opt. Phys.* **26**, 4503 (1993).
- [104] D. Neuhasauer and M. Baer, *J. Chem. Phys.* **90**, 4351 (1989).
- [105] N. Moiseyev, *J. Phys. B: At. Mol. Opt. Phys.* **31**, 1431 (1998).
- [106] J. Muga, J. Palao, B. Navarro, and I. Egusquiza, *Phys. Rep.* **395**, 357 (2004).
- [107] R. J. Maurer, V. G. Ruiz, J. Camarillo-Cisneros, W. Liu, N. Ferri, K. Reuter, and A. Tkatchenko, *Prog. Surf. Sci.* **91**, 72 (2016).
- [108] F. Aguilar-Galindo, M. Zapata-Herrera, S. Díaz-Tendero, J. Aizpurua, and A. G. Borisov, *ACS Photon.* **8**, 3495 (2021).
- [109] F. Flores, J. Ortega, and H. Vázquez, *Phys. Chem. Chem. Phys.* **11**, 8658 (2009).
- [110] I. Scivetti and M. Persson, *J. Phys.: Condens. Matter* **29**, 355002 (2017).
- [111] M. Imai-Imada, H. Imada, K. Miwa, J. Jung, T. K. Shimizu, M. Kawai, and Y. Kim, *Phys. Rev. B* **98**, 201403(R) (2018).
- [112] J. M. Garcia-Lastra, C. Rostgaard, A. Rubio, and K. S. Thygesen, *Phys. Rev. B* **80**, 245427 (2009).
- [113] J. Ziroff, F. Forster, A. Schöll, P. Puschnig, and F. Reinert, *Phys. Rev. Lett.* **104**, 233004 (2010).
- [114] K. A. Cochran, A. Schiffrin, T. S. Roussy, M. Capsoni, and S. A. Burke, *Nat. Commun.* **6**, 8312 (2015).
- [115] R. Bennewitz, V. Barwoff, M. Bammerlin, C. Loppacher, M. Guggisberg, A. Baratoff, E. Meyer, and H.-J. Güntherodt, *Surf. Sci.* **438**, 289 (1999).
- [116] F. Olsson and M. Persson, *Surf. Sci.* **540**, 172 (2003).

- [117] W. Steurer, L. Gross, and G. Meyer, *Appl. Phys. Lett.* **104**, 231606 (2014).
- [118] P. Jakob and S. Thussing, *Phys. Rev. Lett.* **126**, 116801 (2021).
- [119] P. Nordlander and J. Tully, *Surf. Sci.* **211-212**, 207 (1989).
- [120] A. G. Borisov, D. Teillet-Billy, J. P. Gauyacq, H. Winter, and G. Dierkes, *Phys. Rev. B* **54**, 17166 (1996).
- [121] J. Gadzuk, *Surf. Sci.* **6**, 133 (1967).
- [122] J. Gadzuk, *Surf. Sci.* **6**, 159 (1967).